Computational and Spectroscopic Studies of New Rhenium(I) Complexes Containing Pyridylimidazo[1,5-*a*]pyridine Ligands: Charge Transfer and Dual Emission by Fine-Tuning of Excited States

Luca Salassa,[†] Claudio Garino,[†] Andrea Albertino,[†] Giorgio Volpi,[†] Carlo Nervi,[†] Roberto Gobetto,*[,†] and Kenneth I. Hardcastle[‡]

Dipartimento di Chimica IFM, Università di Torino, Via P. Giuria 7, I-10125 Torino, Italy, and Department of Chemistry, Emory University, 1515 Dickey Drive, Atlanta, Georgia 30322

Received November 23, 2007

Three new $Re(CO)_3Cl$ complexes (**ReL1**−**ReL3**) containing the *N*,*N*-bidentate ligands 1-(2-pyridyl)-3-phenylimidazo[1,5-*a*]pyridine (**L1**), 1-(2-pyridyl)-3-(4-*tert*-butylphenyl)imidazo[1,5-*a*]pyridine (**L2**), and 1-(2-pyridyl)-3-(4-dimethylaminophenyl)imidazo[1,5-*a*]pyridine (**L3**) were synthetized and fully characterized. Photophysical properties of **L1**−**L3** and **ReL1**−**ReL3** were studied with absorption and emission spectroscopy. The X-ray structure of **ReL3** was determined. Time-dependent DFT (TDDFT) calculations were performed in order to elucidate the electronic structures and the excited states of ligands and complexes. Ligands **L1** and **L2** show $^1\pi-\pi^*$ emission with limited charge-transfer character (CT), while **L3** emits from an excited state with higher CT character due to the presence of a dimethylamino group. No emissive metal-to-ligand charge-transfer (MLCT) states are found for the rhenium complexes. **ReL1** and **ReL2**, although similar to their ligands, display a ligand-centered $^1\pi-\pi^*/^3\pi-\pi^*$ dual emission; singlet emissions fall at 21.8×10^3 (458 nm) and 22.6×10^3 cm^{-1} (443 nm), respectively, and the structured triplet emissions have two peaks at 17.9×10^3 (558 nm) and 16.3×10^3 cm^{-1} (613 nm) in both complexes. **ReL3** emits from a ligand-centered CT state at 18.9×10^3 cm^{-1} (530 nm). Finally, the complex $[Re(\mathbf{L1})(CO)_3py]PF_6$ (**ReL1py**) (where py = pyridine) was prepared and studied by spectroscopy and computational methods. The complex has high-energy emission centered at 22.9×10^3 cm^{-1} (437 nm). DFT calculations show that dual fluorescence almost disappears due to the reduced spin–orbit coupling. Finally, electrochemical properties of ligands and rhenium complexes have been investigated.

Introduction

The demand for optically functional materials prompts researchers to design new ligands and metal complexes. This search is driven by the need to control excited states and photophysical features for applications such as solar cells,[1] OLEDs,[2] molecular sensors and probes,[3] DNA intercalators,[4] and supramolecular structures.[5] Together with new synthetic methods, computation plays a crucial role in the development of these devices. Among computational methods, time-dependent DFT (TDDFT) is a fundamental tool in understanding and describing singlet and triplet excited states,[6,7] absorption and emission properties,[8] photoactivation processes,[9] and light-induced charge transfer.[10,11]

The design of novel materials for OLED applications needs to satisfy well-defined requirements in terms of emission wavelength (λ_{em}), lifetime (τ), and quantum yields (φ).[12,13] Blue emitters (450–470 nm) are still the most challenging because of their tradeoff between wavelength and emission intensity and lifetime. The critical characteristic of blue light emitters for use in OLED applications is the admixture between metal orbitals and ligand orbitals. In principle, MLCT character increase of the emitting state can be considered a general way to improve quantum yield and, consequently, performance. However, the design of molecules with ideal characteristics is not straightforward; mixing of excited states or predominance of $\pi-\pi^*$ and LLCT character can be obtained in metal complexes. Upon increasing emission energy, the admixture between the two sets of orbitals is generally decreased such that spin–orbit coupling and intersystem crossing are reduced. The result is a decrease in the emission efficiency, due to the decrease of radiative decay

* Corresponding author. E-mail: roberto.gobetto@unito.it.
[†] Università di Torino.
[‡] Emory University.

(1) Nazeeruddin, Md. K.; Kay, A.; Rodicio, I.; Humphry-Baker, R.; Müller, E.; Liska, P.; Vlachopoulos, N.; Grätzel, M. *J. Am. Chem. Soc.* **1993**, *115*, 6382–6390.
(2) Chou, P.-T.; Chi, Y. *Eur. J. Inorg. Chem.* **2006**, 3319–3332.
(3) Demas, J. N.; Degraff, B. A. *J. Chem. Educ.* **1997**, 690–695.
(4) Jenkins, Y.; Friedman, A. E.; Turro, N. J.; Barton, J. K. *Biochemistry* **1992**, *31*, 10809–10816.
(5) Schlicke, B.; De Cola, L.; Belser, P.; Balzani, V. *Coord. Chem. Rev.* **2000**, 267–275.
(6) Batista, E. R.; Martin, R. L. *J. Phys. Chem. A* **2005**, *109*, 3128–3133.
(7) Fantacci, S.; De Angelis, F.; Selloni, A. *J. Am. Chem. Soc.* **2003**, *125*, 4381–4387.
(8) Browne, W. R.; O'Boyle, N. M.; McGarvey, J. J.; Vos, J. G. *Chem. Soc. Rev.* **2005**, *34*, 641–663.
(9) Vlček, A.; Záliš, S. *Coord. Chem. Rev.* **2007**, *251*, 258–287.
(10) Maus, M.; Retting, W.; Bonafoux, D.; Lapouyade, R. *J. Phys. Chem. A* **1999**, *103*, 3388–3401.
(11) El-Gezawy, H.; Retting, W.; Lapouyade, R. *J. Phys. Chem. A* **2006**, *110*, 67–75.
(12) Chou, P.-T.; Chi, Y. *Chem.−Eur. J.* **2007**, *13*, 380–395.
(13) Evans, R. C.; Douglas, P.; Winscom, C. J. *Coord. Chem. Rev.* **2006**, *250*, 2093–2126.

10.1021/om701175z CCC: $40.75
Publication on Web 03/04/2008

Scheme 1

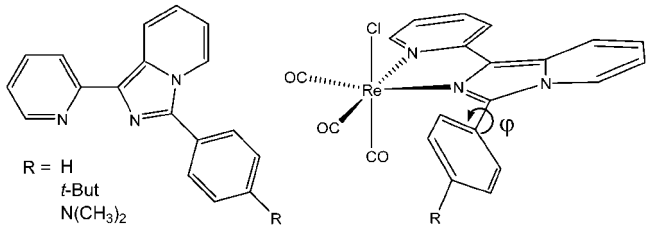

rate (k_r) and decrease in quantum yield as well. However, the metal and ligand mixing can be fine-tuned by varying metal, ligands, and substituents within the molecule's basic structure. Spin–orbit coupling can also be improved, leading to efficient intersystem crossing that increases phosphorescence.

The structurally diverse *N*,*N*-bidentate ligands with mixed five- and six-membered heterocycles have raised interest as a new class of ligands for optical applications.[14,15] We studied the photophysical properties of three 1-pyridylimidazo[1,5-*a*]pyridine with varied substituents in position 3: phenyl (**L1**), 4-*tert*-butylphenyl (**L2**), and 4-dimethylaminophenyl (**L3**) (Scheme 1). We also investigated the effect of metal coordination on absorption and emission properties of the ligands using the $ReL(CO)_3$ unit and employing spectroscopic and computational methods. $[ReL(CO)_3X]$ complexes have been extensively studied for applications in OLEDs[16,17] and in other fields such as solar energy conversion,[18] supramolecular chemistry,[19] catalysis,[20] and medical chemistry.[21] Three new rhenium derivatives were prepared for this reason: [Re**L1**$(CO)_3$Cl] (**ReL1**), [Re**L2**$(CO)_3$Cl] (**ReL2**), [Re**L3**$(CO)_3$Cl] (**ReL3**). Finally the complex [Re(**L1**)$(CO)_3$py]PF_6 (**ReL1py**) (where py = pyridine) was synthesized and studied in order to evaluate the effect of an electron-donating ligand on the complex. The proposed comparative study among ligands and complexes will be a useful example of how excited states and optical properties can be regulated and fine-tuned by selected structural changes.

Experimental Section

Materials and Reagents. All solvents in the synthetic procedures were of analytical reagent grade and purified according to literature procedures.[22] $Re(CO)_5Cl$, 2,2′-dipyridyl ketone, benzaldehyde, 4-*tert*-butilbenzaldehyde, 4-dimethylaminobenzaldehyde, ammonium acetate, calcium hydride, tetrabutylammonium hexafluorophosphate, pyridine, and tetrabutylammonium iodide Na_2SO_4, NaCl, $NaHCO_3$, KPF_6, $AgNO_3$, were purchased from Aldrich and used as received without further purification.

Physical Methods. NMR spectra were recorded on a JEOL EX 400 spectrometer (B_0 = 9.4 T, ^{1}H operating frequency 399.78 MHz) with chemical shifts referenced to residual protons in the solvent (acetone-d_6, DMSO-d_6, or acetonitrile-d_3). Infrared spectra were obtained as KBr pellets using a Bruker Equinox 55 FT-IR spectrophotometer, with a resolution of 1 cm^{-1} and an accumulation of 64 scans.

UV–vis absorption spectra were measured with a double-beam Perkin-Elmer Lambda 20 UV–visible spectrophotometer equipped with a 1 cm quartz cell. Room-temperature emission spectra as well as luminescence lifetimes were obtained using a HORIBA Jobin Yvon IBH Fluorolog-TCSPC spectrofluorimeter. Fluorescence quantum yields φ were determined using quinine bisulfate (0.1 N H_2SO_4) as standard (φ = 0.546).[23] Refractive index corrections were made to adjust for different solvents used. Luminescence lifetimes were determined by time-correlated single-photon counting. Excitation with nanosecond pulses of 297 nm light (repetition rates ranging from 1 MHz to 10 kHz) generated by a NanoLED pulsed diode was used for lifetimes shorter than 100 μs, while lifetimes longer than 100 μs were evaluated using 100 ns pulses of 375 nm light generated by a SpectraLED pulsed diode. The emission data were collected using a spectral bandwidth of 10 nm. The data were collected into 2048 channels to 10 000 counts in the peak channel. The sample was maintained at 20 °C in an automated sample chamber (F-3004 Peltier sample cooler from Horiba Jobin Yvon IBH) for ambient temperature measurements. Emission decay data were analyzed using the software DAS6 (TCSPC decay analysis software). Decays longer than 1 μs were fit directly without reconvolution as sums of exponentials assuming that the excitation pulse is a delta function at this time resolution. Decays shorter than 1 μs were fit with reconvolution of the time-dependent profile of the light source. The best fit was assessed based on the parameter χ^2, which was close to 1.0 for all the samples, and the distribution of weighted residual along the zero line. Mass spectra were recorded using an XCT PLUS electrospray ionization-ion trap (ESI-IT) mass spectrometer (Agilent Italy, Milan). Samples were dissolved in methanol/water (9:1) solution with 0.1% of formic acid. Scan range was 200–800 *m*/*z*.

X-ray Structure Determination. A suitable crystal of [Re(1-(2-pyridyl)-3-(4-dimethylaminophenyl)imidazo[1,5-*a*]pyridine)$(CO)_3$Cl] (**ReL3**) was coated with Paratone N oil, suspended in a small fiber loop, and placed in a cooled nitrogen gas stream at 173 K on a Bruker D8 SMART APEX CCD sealed tube diffractometer with graphite-monochromated Mo Kα (0.71073 Å) radiation. Data were measured using a series of combined phi and omega scans with 10 s frame exposures and 0.3° frame widths. Data collection, indexing, and initial cell refinements were all carried out using SMART[24] software. Frame integration and final cell refinements were done using SAINT[25] software. The final cell parameters were determined from least-squares refinement on 12 809 reflections. The SADABS[26] program was used to carry out absorption corrections. The structure was solved using direct methods and difference Fourier techniques (SHELXTL, V6.12).[27] Hydrogen atoms were placed into their expected chemical positions using the HFIX command and were included in the final cycles of least-squares with isotropic U_{ij}'s related to the atom's ridden upon. All non-hydrogen atoms were refined anisotropically. Scattering factors and anomalous dispersion corrections are taken from the *International Tables for X-ray Crystallography*.[28] Structure solution, refinement, graphics, and generation of publication materials were performed by using SHELXTL, V6.12 software.

(14) Ligtenbarg, A. G.; Spek, A. L.; Hage, R.; Feringa, B. L. *J. Chem. Soc., Dalton Trans.* **1999**, 659–661.
(15) Bluhm, M. E.; Ciesielski, M.; Görls, W. O.; Döring, M. *Inorg. Chem.* **2003**, *42*, 8878–8885.
(16) Li, F.; Zhang, G.; Cheng, G.; Feng, J.; Zhao, Y.; Ma, Y. G.; Lui, S. Y.; Shen, J. C. *Appl. Phys. Lett.* **2004**, *84*, 148–150.
(17) Li, Y.; Liu, Y.; Guo, J.; Wu, F.; Tian, W.; Li, B.; Wang, Y. *Synth. Met.* **2001**, *118*, 175–179.
(18) Sarto Polo, A.; Itokazu, M. K.; Iha, N. Y. M. *Coord. Chem. Rev.* **2004**, *248*, 1343–1361.
(19) Sun, S.-S.; Lees, A. J. *J. Am. Chem. Soc.* **2000**, 8956–8967.
(20) Johnson, F. P. A.; George, M. W.; Hartl, F.; Turner, J. J. *Organometallics* **1996**, *15*, 3374–3387.
(21) Alberto, R.; Schibli, R.; Egli, A.; Schubiger, A. P.; Abram, U.; Kaden, T. A. *J. Am. Chem. Soc.* **1998**, *120*, 7987–7988.
(22) Amarengo, W. L. F.; Perrin, D. D. *Purification of Laboratory Chemicals*; Butterworth-Heinemann: Oxford, 1998.
(23) Eaton, D. F. *Pure Appl. Chem.* **1988**, *60*, 1107–1114.
(24) *SMART* Version 5.628; Bruker AXS, Inc.: Madison, WI, 2003.
(25) *SAINT* Version 6.36A; Bruker AXS, Inc.: Madison, WI, 2002.
(26) Sheldrick, G. M. *SADABS* Version 2.10; University of Göttingen: Germany, 2003.
(27) *SHELXTL* V6.12; Bruker AXS, Inc.: Madison, WI, 2002.
(28) Wilson, A. J. C. *International Tables for X-ray Crystallography, Volume C*; Academic Publishers: Dordrecht, 1992; Table 6. 1.1.4, pp 500–502, and Table 4.2.6.8, pp 219−222.

Table 1. Selected Bond Distances (Å) of ReL1−ReL3 in Calculated Ground State Geometries and X-ray Crystallography

	Re−Cl	Re−C(py)	Re−C(im)	Re−C(Cl)	Re−N(py)	Re−N(im)
ReL1	2.528	1.930	1.920	1.916	2.231	2.219
ReL2	2.528	1.930	1.920	1.917	2.231	2.217
ReL3	2.529	1.930	1.920	1.916	2.231	2.217
ReL3 X-ray	2.478(2)	1.921(7)	1.935(8)	1.918(7)	2.188(5)	2.196(5)

Computational Details. Gaussian 03[29] was employed for all the calculations. Geometry optimization calculations of the ground and lowest-lying triplet state in the gas phase were performed with the gradient-corrected correlation functional B3LYP.[30,31] The LanL2DZ basis set and effective core potential were used for the Re atom and the 6-31G** basis set was used for all other atoms, respectively. Ligands were optimized at the B3LYP/6-31G** level. The nature of all stationary points was confirmed by performing a normal-mode analysis.

Eight singlet excited states for **L1**−**L3** and 32 singlet excited states for **ReL1**−**ReL3** and **ReL1py** were calculated with time-dependent DFT (TDDFT) calculation[32,33] employing ground-state geometries optimized in the gas phase.

The conductor-like polarizable continuum model method (CPCM)[34−36] with acetonitrile as solvent was used to calculate all the electronic structure and excited states in solution. The electronic distribution and the localization of the singlet excited states were visualized using the electron density difference maps (EDDMs).[8] GaussSum 1.05[37] was used for EDDMs calculations and for the electronic spectrum simulation. Only electronic transitions with an oscillator strength value (*f*) higher than 0.05 are reported in Table 2 for **ReL1**−**ReL3**. Emission energies were determined employing the Δ_{SCF} approach,[38,39] which calculates the vertical energy gap between the S0 and T1 energies, both evaluated at the optimized geometry of T1.

Electrochemical Measurements. Acetonitrile was distilled over calcium hydride just before use, and tetrabutylammonium hexafluorophosphate was obtained as a metathesis reaction between KPF_6 and tetrabutylammonium iodide, recrystallized three times from 95% ethanol, and dried in a vacuum oven at 110 °C overnight. Electrochemistry was performed with an EG&G PAR 273 electrochemical analyzer controlled by a PC. A standard three-electrode cell was designed to allow the tip of the reference electrode to closely approach the working electrode. The reference electrode was a 3 M KCl calomel electrode, the auxiliary electrode was a platinum wire, and the working electrode was glassy carbon (GC). Positive feedback *iR* compensation was applied routinely. All measurements were carried out under Ar in anhydrous deoxygenated solvents. Ferrocene (Fc) was used as an internal standard, and potentials are reported against the Fc(0/+1) redox couple (measured $E_{1/2}$(0/+1) 0.38 V).

Synthesis of Ligands. The ligands 1-(2-pyridyl)-3-phenylimidazo[1,5-*a*]pyridine (**L1**) and 1-(2-pyridyl)-3-(4-dimethylaminophenyl)imidazo[1,5-*a*]pyridine (**L3**) were prepared according to published procedures.[40]

Synthesis of 1-(2-Pyridyl)-3-(4-*tert*-butylphenyl)imidazo-[1,5-*a*]pyridine (L2). L2 was obtained with a slight modification of a previously published procedure.[40] A mixture consisting of 2,2′-dipyridyl ketone (1.84 g, 10.0 mmol), 4-*tert*-butylbenzaldehyde (3.24 g, 20.0 mmol), and ammonium acetate (3.86 g, 50.0 mmol) in 100 mL of glacial acetic acid was stirred at 110 °C under N_2. After 5 h, the reaction mixture was cooled to room temperature and the acetic acid was removed by evaporation under vacuum.

The solid was dissolved in an aqueous solution of NaCl and $NaHCO_3$ and the mixture extracted with CH_2Cl_2. The organic layer was separated and the solvent was evaporated under vacuum. The formed solid was dried washing three times with ethyl ether. Yield: 78% (2.55 g). ^{1}H NMR (acetone-d_6, ppm) δ: 1.39 (s, 9H), 6.81 (t, $^3J_{HH}$ = 7.2 Hz, 1H), 7.02 (t, $^3J_{HH}$ = 8.0 Hz, 1H), 7.15 (t, $^3J_{HH}$ = 6.2 Hz, 1H), 7.64 (d, $^3J_{HH}$ = 8.8 Hz, 2H), 7.79 (t, $^3J_{HH}$ = 9.1 Hz, 1H), 7.86 (d, $^3J_{HH}$ = 8.0 Hz, 2H), 8.24 (d, $^3J_{HH}$ = 8.4 Hz, 1H), 8.48 (d, $^3J_{HH}$ = 7.2 Hz, 1H) 8.61 (d, $^3J_{HH}$ = 5.0 Hz, 1H), 8.73 (d, $^3J_{HH}$ = 9.1 Hz, 1H). ^{13}C NMR (acetone-d_6, ppm) δ: 31.5, 114.8, 120.2, 121.2, 122.0, 122.4, 123.2, 125.3, 126.4, 126.7, 128.4, 128.8, 129.7, 131.0, 137.0, 149.8, 152.6, 156.3.

General Synthesis of *fac*-Re(L)(CO)$_3$Cl. Chloro complexes, Re(L)(CO)$_3$Cl, were obtained with a slight modification of a previously published procedure;[41] Re(CO)$_5$Cl (0.40 g, 1.1 mmol) was heated at reflux with equimolar quantities of appropriate ligand in toluene for 4 h. The yellow products were precipitated from solution, then filtered and washed with toluene and ethyl ether.

***fac*-Re(L1)(CO)$_3$Cl (ReL1).** Yield: 71% (0.452 g). IR (KBr pellets, cm^{-1}): 2014 (s), 1892 (br). ^{1}H NMR (DMSO-d_6, ppm) δ: 7.08 (t, $^3J_{HH}$ = 6.7 Hz, 1H), 7.44–7.49 (m, 2H), 7.70–7.74 (m, 3H), 7.82–7.84 (m, 2H), 8.14 (d, $^3J_{HH}$ = 7.3 Hz, 1H), 8.18 (t, $^3J_{HH}$ = 7.6 Hz, 1H), 8.48 (d, $^3J_{HH}$ = 8.5 Hz, 2H), 8.90 (d, $^3J_{HH}$ = 5.3 Hz, 1H). ^{13}C NMR (DMSO-d_6, ppm) δ: 116.2, 117.3, 120.8, 123.4, 124.0, 126.2, 126.4, 129.0, 129.3, 131.0, 131.3, 139.8, 140.4, 152.5, 152.7, 195.6, 197.8. MS: *m*/*z* 574 (M^+ − Cl + CH_3OH), *m*/*z* 542 (M^+ − Cl). Anal. Calcd. for $C_{21}H_{13}ClN_3O_3Re$: C 43.71; H 2.27; N 7.28. Found: C 43.75; H 2.10; N 7.09.

***fac*-Re(L2)(CO)$_3$Cl (ReL2).** Yield: 75% (0.525 g). IR (KBr pellets, cm^{-1}): 2021 (s), 1921 (br). ^{1}H NMR (DMSO-d_6, ppm) δ: 1.36 (s, 9H), 7.07 (t, $^3J_{HH}$ = 7.0 Hz, 1H), 7.49–7.43 (m, 2H), 8.15–8.20 (m, 2H), 8.47 (d, $^3J_{HH}$ = 8.8 Hz, 2H), 8.88 (d, $^3J_{HH}$ = 5.4 Hz, 1H). ^{13}C NMR (DMSO-d_6, ppm) δ: 30.8, 34.8, 116.1, 117.3, 120.8, 123.4, 124.1, 126.1, 126.4, 129.0, 130.6, 139.7, 140.5, 152.6, 152.7, 154.1. MS: *m*/*z* 630 (M^+ − Cl + CH_3OH), *m*/*z* 598 (M^+ − Cl). Anal. Calcd for $C_{25}H_{21}ClN_3O_3Re$: C 47.43; H 3.34; N 6.64. Found: C 47.56; H 3.22; N 6.49.

***fac*-Re(L3)(CO)$_3$Cl (ReL3).** Yield: 68% (0.466 g). IR (KBr pellets, cm^{-1}): 2013 (s), 1910 (br). ^{1}H NMR (DMSO-d_6, ppm) δ: 3.04 (s, 6H), 6.96 (d, $^3J_{HH}$ = 9.1 Hz, 2H), 7.043 (t, $^3J_{HH}$ = 7.0, 1H), 7.43 (q, $^3J_{HH}$ = 10.4 Hz, 2H), 7.60 (d, $^3J_{HH}$ = 9.1, 2H), 8.15

(29) Frisch, M. J.; Trucks, G. W.; Schlegel, H. B.; Scuseria, G. E.; Robb, M. A.; Cheeseman, J. R.; Montgomery, J. A., Jr., Vreven, T.; Kudin, K. N.; Burant, J. C.; Millam, J. M.; Iyengar, S. S.; Tomasi, J.; Barone, V.; Mennucci, B.; Cossi, M.; Scalmani, G.; Rega, N.; Petersson, G. A.; Nakatsuji, H.; Hada, M.; Ehara, M.; Toyota, K.; Fukuda, R.; Hasegawa, J.; Ishida, M.; Nakajima, T.; Honda, Y.; Kitao, O.; Nakai, H.; Klene, M.; Li, X.; Knox, J. E.; Hratchian, H. P.; Cross, J. B.; Adamo, C.; Jaramillo, J.; Gomperts, R.; Stratmann, R. E.; Yazyev, O.; Austin, A. J.; Cammi, R.; Pomelli, C.; Ochterski, J.; Ayala, P. Y.; Morokuma, K.; Voth, G. A.; Salvador, P.; Dannenberg, J. J.; Zakrzewski, V. G.; Dapprich, S.; Daniels, A. D.; Strain, M. C.; Farkas, O. , Malick, D. K.; Rabuck, A. D.; Raghavachari, K.; Forestman, J. B.; Ortiz, J. V.; Cui, Q.; Baboul, A. G.; Clifford, S.; Cioslowski, J.; Stefanov, B. B.; Liu, G.; Liashenko, A.; Piskorz, P.; Komaromi, I.; Martin, R. L.; Fox, D. J.; Keith, T.; Al-Laham, M. A.; Peng, C. Y.; Nanayakkara, A.; Challacombe, M.; Gill, P. M. W.; Johnson, B.; Chen, W.; Wong, M. W.; Gonzales, C., Pople, J. A. *Gaussian 03 (revision C.02)*; Gaussian Inc.: Wallingford, CT, 2004.

(30) Becke, A. D. *J. Chem. Phys.* **1993**, *98*, 5648–5652.

(31) Lee, C.; Yang, W.; Parr, R. G. *Phys. Rev. B: Condens. Matter* **1988**, *37*, 785–789.

(32) Casida, M. E.; Jamorski, C.; Casida, K. C.; Salahub, D. R. *J. Chem. Phys.* **1998**, *108*, 4439–4449.

(33) Stratmann, R. E.; Scuseria, G. E.; Frisch, M. J. *J. Chem. Phys.* **1998**, *109*, 8218–8224.

(34) Barone, V.; Cossi, M. *J. Phys. Chem. A* **1998**, *102*, 1995–2001.

(35) Cossi, M.; Rega, N.; Scalmani, G.; Barone, V. *J. Comput. Chem.* **2003**, *24*, 669–681.

(36) Cossi, M.; Barone, V. *J. Chem. Phys.* **2001**, *115*, 4708–4717.

(37) O'Boyle, N. M.; Vos, J. G. *GaussSum* (1.0). Dublin City University, 2005. Available at http://gausssum.sourceforge.net.

(38) Ziegler, T.; Rauk, A.; Baerends, E. J. *Theor. Chim. Acta* **1977**, *43*, 261–271.

(39) Daul, C. *Int. J. Quantum Chem.* **1994**, *52*, 867–877.

(40) Wang, J.; Dyers, L.; Mason, R.; Amoyaw, P.; Bu, X. R. *J. Org. Chem.* **2005**, *70*, 2353–2356.

(41) Caspar, J. V.; Meyer, T. J. *J. Phys. Chem. A* **1983**, *87*, 952–957.

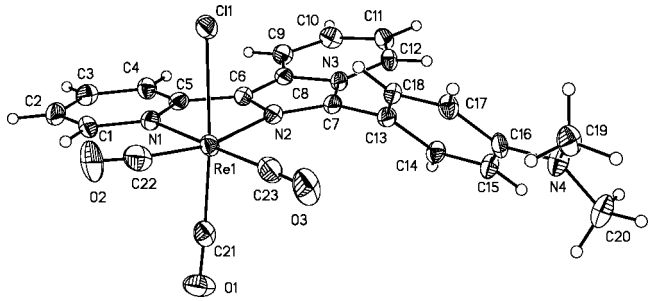

Figure 1. X-ray structure of **ReL3** showing the adopted labeling scheme, with displacement ellipsoids drawn at 30% probability.

(m, 2H), 8.43 (q, $^3J_{HH}$ = 9.1 Hz, 2H), 8.88 (d, $^3J_{HH}$ = 5.9 Hz, 1H). ^{13}C NMR (DMSO-d_6, ppm) δ: 111.9, 112.2, 115.8, 117.3, 120.6, 123.2, 124.0, 126.1, 128.9, 131.7, 139.6, 141.5, 151.8, 152.6, 152.7. MS: *m/z* 617 (M^+ − Cl + CH_3OH), *m/z* 585 (M^+ − Cl). Anal. Calcd for $C_{23}H_{18}ClN_4O_3Re$: C 44.55; H 2.92; N 9.04. Found: C 44.47; H 3.11; N 8.96.

Synthesis of *fac*-[Re(L1)(CO)$_3$(py)][PF$_6$] (ReL1py). A mixture of **ReL1** (0.5 mmol) and $AgNO_3$ (20% excess) was dissolved in CH_3CN. The reaction solution was refluxed overnight in the dark, under argon atmosphere. The resulting mixture was cooled to room temperature, and the precipitated AgCl was removed by filtration. The acetonitrile intermediate *fac*-[Re(**L1**)(CO)$_3$(CH_3CN)]$^+$ was then precipitated from the resulting solution as hexafluorophosphate salt by adding an aqueous solution of NH_4PF_6 and removing the solvent by evaporation under vacuum. The complex obtained was dissolved in THF and heated to reflux with an excess of pyridine (40:1) under an argon atmosphere for 2 h. The solution was cooled to room temperature, and the yellowish solid was precipitated by adding 100 mL of pentane and then filtered. Yield: 62% (0.197 g). IR (KBr pellets, cm^{-1}): 2026 (s), 1902 (br). ^{1}H NMR (acetonitrile-d_3, ppm) δ: 7.02 (t, $^3J_{HH}$ = 6.9 Hz, $^4J_{HH}$ = 0.9 Hz, 1H), 7.29 (t, $^3J_{HH}$ = 7.0 Hz, 2H), 7.40–7.48 (m, 2H), 7.61, (t, $^3J_{HH}$ = 7.0 Hz, 2H), 7.74 (s, br, 5H), 7.84 (t, $^3J_{HH}$ = 7.6 Hz, $^4J_{HH}$ = 1.5 Hz, 1H), 8.01–8.16 (m, 4H), 8.60 (d, $^3J_{HH}$ = 4.7 Hz, 1H), 9.08 (d, $^3J_{HH}$ = 5.3 Hz, 1H). ^{13}C NMR (acetonitrile-d_3, ppm) δ: 116.4, 117.0, 117.4, 121.1, 124.2, 124.6, 125.4, 126.3, 126.8, 127.2, 129.1, 129.9, 130.5, 132.1, 139.7, 140.4, 140.7, 141.8, 147.4, 152.2, 153.4, 153.6, 192.6, 194.1, 196.0. MS: *m/z* 621 (M^+). Anal. Calcd for $C_{26}H_{18}F_6N_4O_3PRe$: C 40.79; H 2.37; N 7.32. Found: C 40.84; H 2.41; N 7.24.

Results and Discussion

Computed Geometries and X-ray Structures. The three 1-pyridylimidazo[1,5-*a*]pyridine ligands display similar structural features; in all computed geometries, the pyridyl moiety in position 1 is coplanar with the imidazo[1,5-*a*]pyridine rings and has *trans* conformation. The phenyl groups are rotated relative to the imidazo[1,5-*a*]pyridine plane by 36.5°, 37.2°, and 38.3° in **L1**, **L2**, and **L3**, respectively.

DFT calculations on **ReL1**, **ReL2**, and **ReL3** show how the planarity of the ligands is maintained also upon coordination. Phenyl substituents in the three models are further rotated for minimizing steric interaction with the CO group *trans* to the 1-pyridyl ring. The calculated rotational angles for the phenyl groups are 60.2°, 57.1°, and 55.4° for **ReL1**, **ReL2**, and **ReL3**, respectively. The X-ray structure of **ReL3** is reported in Figure 1; a comparison of selected bond lengths with computed geometries is presented in Table 1. Crystallographic data for the X-ray structure can be found in the Supporting Information.

Interestingly, the X-ray structure shows the Re(CO)$_3$ unit as orthogonal, but rotated with respect to the ligand plane, having the dihedral angle C1−N1−Re1−C22 of –11.2°; a space-filling figure indicates that this is due to steric crowding by the pendant phenyl substituent (Figure 2).

Table 2. Absorption and Emission Properties of L1−L3, ReL1−ReL3, and ReL1py in Acetonitrile

	λ_{abs}, nm	ϵ, M^{-1} cm^{-1}	ν_{em}, × 10^3 cm^{-1} (nm)	φ	τ, ns
L1	323	19 072	21.9 (456)	0.21	4.8
	377	9783			
L2	320	14 363	21.8 (458)	0.21	4.6
	381	6100			
L3	274	14 259	20.1 (498)	0.12	3.6
	322	25 460			
	388	5966			
ReL1	291	13 300	21.8 (458)	∼10^{-4}	6.3
	378	14 000	17.9 (558)		∼1.3 ms
			16.3 (613)		
ReL2	291	16 300	22.6 (443)	∼10^{-4}	5.1
	381	16 600	17.8 (561)		∼0.2 ms
			16.3 (612)		
ReL3	297	24 200	18.9 (530)	0.0023	3.9
	388	13 800			
ReL1py	290	13 800	22.9 (437)	∼10^{-4}	5.8
	379	12 200	17.9 (559)		

Orbital Analysis. The three ligands have similar HOMO and LUMO orbitals. The HOMO is an antibonding π orbital delocalized over the whole molecule. No contribution from the 4-*tert*-butyl group is present in **L2**, while a consistent contribution from the dimethylamino group (dma) is present in **L3**. Only in the case of **L3** is there overlapping between dma-phenyl orbitals and imidazo[1,5-*a*]pyridine orbitals. The LUMOs are all π*, localized only on the 1-pyridylimidazo[1,5-*a*]pyridine portion. The HOMO–LUMO energy gaps are respectively 3.81, 3.78, and 3.54 eV for **L1**, **L2**, and **L3**.

L1 and **L2** have occupied frontier orbitals that are π* in most cases, either localized on the whole molecule or on part of it. HOMO−2 and HOMO−3 also have an n−π* character localized on the pyridine moiety. Unoccupied orbitals for these two ligands are all predominantly π*. **L3** presents similar occupied frontier orbitals, but has more in-phase overlapping on the imidazo[1,5-*a*]pyridine (for example, HOMO−1 and HOMO−5) than the other ligands. HOMO−2 and HOMO−3 have n−π* character in this case as well.

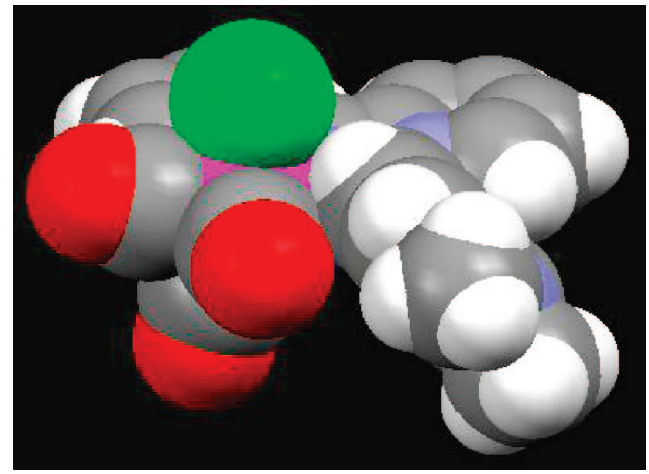

Figure 2. Space-filling representation of the solid state molecular structure of **ReL3**.

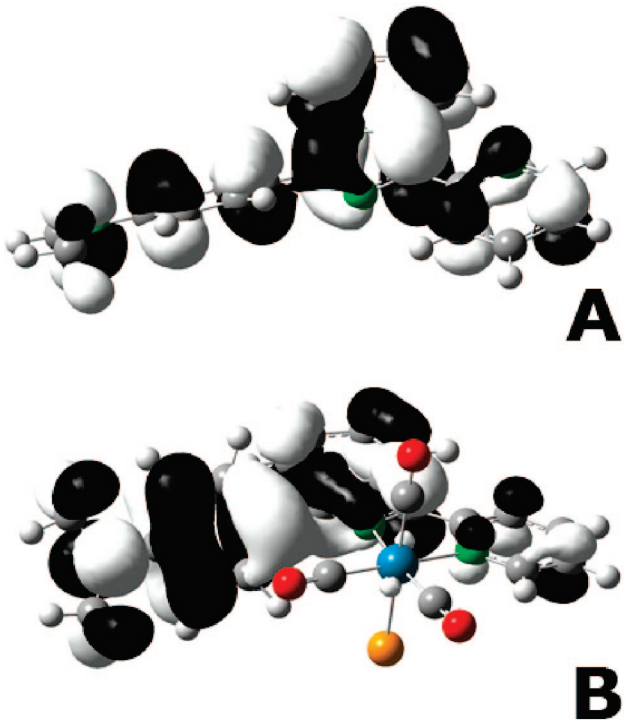

Figure 3. HOMO representation for **L3** (A) and **ReL3** (B).

ReL1 and **ReL2** have π^* HOMOs, which substantially resemble the free ligands, although there is a back-donation contribution from the metal, particularly toward the imidazo[1,5-*a*]pyridine rings. **ReL3** has relevant differences in the HOMO with respect to **L3** and the other two rhenium derivatives. The orbital components of the dma-phenyl and imidazo[1,5-*a*]pyridine moieties overlap significantly more than the other compounds (Figure 3), affecting **L3**'s spectroscopic properties. Furthermore, no metal contribution is observed at all for this complex. In contrast, LUMOs are identical for the three rhenium complexes; π^* orbitals are localized on the chelating part of the ligand with some contribution from the Cl and CO orbitals. The HOMO–LUMO energy gaps of the rhenium complexes follow the same trend of the organic ligands. From **ReL1** to **ReL2** and **ReL3**, the energy changes from 3.73 to 3.70 and 3.32 eV. The metal coordination slightly increases the difference in energy between **L3** and the other ligands, due to the increased energy of its HOMO. The orbitals HOMO−1, HOMO−2, and HOMO−3 have similar features for the three derivatives. This set of orbitals is centered on the $Re(CO)_3Cl$ core. The only exception is HOMO−1 for **ReL3**, which is still primarily ligand-based.

HOMO−4 is phenyl- (or *tert*-butylphenyl-) based for **ReL1** to **ReL2**, while it is basically $Re(CO)_{eq}$-based for **ReL3**. HOMO−5 is phenyl-centered for all three derivatives.

LUMO+1 and LUMO+2 are all ligand-based. LUMO+3 is π^* for **ReL1** and **ReL2**, but is centered on the Re core for **ReL3**. The chelating part of the ligand contributes to a sigma interaction. LUMO+4 and LUMO+5 are metal-carbonyl-based with a significant contribution from the phenyl ring (LUMO+5).

Absorption and Fluorescence Spectra and Singlet Excited States of L1, L2, and L3. Steady state spectra of the ligands were recorded in hexane and acetonitrile (Figure 4). Singlet excited state calculations were performed with the TDDFT[32,33] method in acetonitrile using Gaussian 03. Results are summarized in Table 3 and Figure 4.

In both **L1** and **L2**, the main absorption band is centered around 320 nm and is composed by two electronic transitions with charge-transfer character (CT). The first transition is a nearly pure CT from the 1-pyridylimidazo[1,5-*a*]pyridine to the phenyl or 4-*tert*-butylphenyl moiety, while the second transition is a mixed $\pi-\pi^*$/CT state, where the $\pi-\pi^*$ state is localized on the central imidazo[1,5-*a*]pyridine ring. Both ligands also have low-energy bands (shoulder at 373 nm) that can be ascribed to a $\pi-\pi^*$ state where there is a partial migration of electronic density from the phenyl (or 4-*tert*-butylphenyl) group to the imidazo[1,5-*a*]pyridine rings. Absorption spectra are largely independent from solvent polarity, except for a decrease in the intensity of the low-energy band moving from hexane to acetonitrile.

L3 displays slightly different absorption properties; the major band centered at 322 nm is the result of a $\pi-\pi^*$/CT state, where the $\pi-\pi^*$ character dominates and the dimethylamino group partially contributes. A high-energy band appears at 274 nm and can be assigned to another mixed state. The shoulder at 388 nm is red-shifted with respect to the other ligands, still with mixed character, but the CT contribution is now more important because of a higher dma contribution. No solvatochromic effect is observed in the absorption spectrum of **L3**.

Comparing the absorption spectra of **L3** and **L1**, no shift in the low-energy bands is observed, indicating that π-electron delocalization from the dimethylamino to the other rings is not significant in the ground state. To illustrate, this shift was 4300 cm^{-1} for biphenyl and 4-dimethylaminobiphenyl.[42]

L1 and **L2** have emission maxima that are independent of solvent polarity and fall at 21.9×10^3 (456 nm) and 21.8×10^3 cm^{-1} (458 nm), respectively. In hexane the bands have vibrational resolution due to the C=C and C=N stretching modes ($\Delta\nu = 1321$ cm^{-1}). **L3** also shows a structured emission at 21.0×10^3 cm^{-1} (476 nm) in hexane; in acetonitrile the emission is further red-shifted at 20.1×10^3 cm^{-1} (498 nm) and unstructured. The increased Stokes shift of **L3** (5126 cm^{-1} in hexane and 6098 cm^{-1} in acetonitrile) compared to **L1** and **L2** confirms the greater CT contribution to the transition with respect to the other ligands (~4700 cm^{-1}). This solvatochromism proves the considerable electron-transfer character of the emitting state of **L3**.

Lifetimes of the three species were measured in acetonitrile. They have single-exponential decays; τ and quantum yield values, reported in Table 2, confirm the proposed assignments.

Absorption and Fluorescence Spectra and Singlet Excited States of ReL1, ReL2, and ReL3. Absorption and emission spectra of the three rhenium complexes were recorded in acetonitrile (Figure 4, Table 2); 32 singlet excited states were calculated with the TDDFT method using Gaussian 03 as described in the Computational Details section.

ReL1 and **ReL2** display two maxima at about 291 and 380 nm in the absorption spectra. According to calculations, the first band is due to high-energy MLCT or MLCT/$\pi-\pi^*$ states. The latter is due to $\pi-\pi^*$ states with a small charge-transfer contribution from the phenyl or 4-*tert*-butylphenyl group of the ligands **L1** and **L2**. It is worth noting that some MLCT character is present in this state as well (EDDMs in Figure 4).

ReL3 has a quite different absorption spectrum. The high-energy band is composed by states with LMCT and MLCT character. The lowest energy absorption band is a pure CT state from the dma-phenyl moiety to the 1-pyridylimidazo[1,5-

(42) Zhu, Y.; Schuster, G. B. *J. Am. Chem. Soc.* **1990**, *112*, 8583–8585.

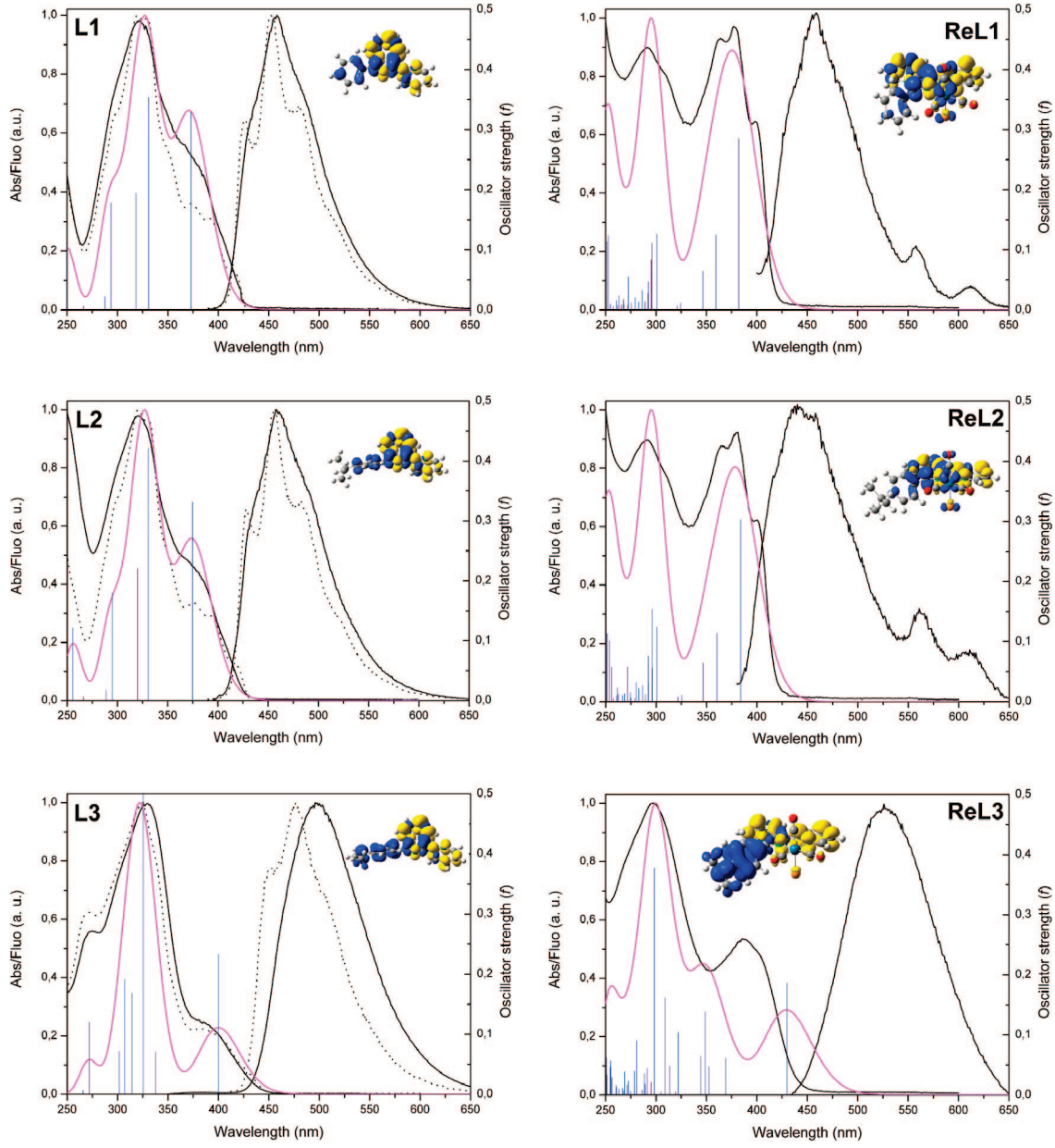

Figure 4. Room-temperature absorption and emission spectra for **L1**−**L3** in hexane (dashed black line) and acetonitrile (solid black line) and for **ReL1**−**ReL3** in acetonitrile (black line). Calculated absorption spectra for **L1**−**L3** and **ReL1**−**ReL3** in acetonitrile (magenta line). The excited states are shown as vertical bars with height equal to the extinction coefficient. Inset: Electron density difference maps (EDDMs) of the lowest energy singlet electronic transition for each ligand and complex (blue indicates a decrease in charge density, while yellow indicates an increase). Theoretical curves and EDDMs were obtained using the program GAUSSSUM 1.05.

a]pyridine.[43,44] Interestingly, no metal contribution is present at all, and the $\pi-\pi^*$ character present in **L3** has almost disappeared in the complex. DFT calculations at the level employed underestimate the energy of this band.

All three complexes have singlet major emissions with low quantum yields involving orbitals that are mainly ligand-centered. Emission lifetimes measurements show τ values of the same magnitude of the ligand ones, indicating their singlet nature. Moreover, **ReL1** and **ReL2** possess a dual fluorescence. They have $^1\pi-\pi^*$ emission bands at 21.8 × 10^3 cm^{-1} (458 nm) for **ReL1** and 22.6 × 10^3 cm^{-1} (443 nm) for **ReL2**. **ReL1** has another two emission maxima, at 17.9 × 10^3 (558 nm) and 16.3 × 10^3 cm^{-1} (613 nm), while the corresponding maxima from **ReL2** fall at 17.8 × 10^3 (561 nm) and 16.3 × 10^3 cm^{-1} (613 nm). These two low-energy emissions can be ascribed to a $^3\pi-\pi^*$ triplet state (peak separation ∼1485 cm^{-1}), as confirmed by the very long lifetime. The lowest-lying triplet state is correctly predicted by DFT, being of $\pi-\pi^*$ character, but the emission energy values calculated with the Δ_{SCF} method[38,39] in the gas phase are underestimated (693 nm for **ReL1** and 697 nm for **ReL2**). Observation of triplet emissions may be facilitated by the low quantum yield of the complexes.

(43) De Angelis, F.; Fantacci, S.; Evans, N.; Klein, C.; Zakeeruddin, S. M.; Moser, J. E.; Kalyanasundaram, K.; Bolink, H. J.; Grätzel, M.; Nazeeruddin, M. K. *Inorg. Chem.* **2007**, *46*, 5989–6001.

(44) Dragonetti, C.; Falciola, L.; Mussini, P.; Righetto, S.; Roberto, D.; Ugo, R.; Valore, A.; De Angelis, F.; Fantacci, S.; Sgamellotti, A.; Ramon, M.; Muccini, M. *Inorg. Chem.* **2007**, *46*, 8533–8547.

(45) Ley, K. D.; Li, Y.; Johnson, J. V.; Powell, D. H.; Schanze, K. S. *Chem. Commun.* **1999**, 1749–1750.

(46) Ley, K. D.; Schanze, K. S. *Coord. Chem. Rev.* **1998**, *171*, 287–307.

Table 3. Calculated Singlet Excited States for L1−L3, ReL1−ReL3, and ReL1py in Acetonitrile

	trans.	E^{calc}, eV (nm)	f	major contribution	character
L1	1	3.32 (373)	0.32	HOMO→LUMO (82%)	$\pi-\pi^*$/CT
	2	3.74 (331)	0.35	HOMO→L+1 (88%)	CT
	3	3.89 (318)	0.19	HOMO→L+2 (90%)	$\pi-\pi^*$/CT
	4	4.22 (294)	0.17	HOMO→L+3 (88%)	CT
	5	4.31 (288)	0.02	HOMO→L+4 (94%)	CT
	6	4.65 (266)	0	HOMO–3→LUMO (69%)	π-π^*/CT
	7	4.96 (250)	0.1	HOMO–1→LUMO (87%)	CT
	8	5.13 (242)	0	HOMO–2→LUMO (77%)	mixed
L2	1	3.31 (375)	0.32	HOMO→LUMO (82%)	π-π^*/CT
	2	3.75 (330)	0.42	HOMO→L+1 (88%)	CT
	3	3.87 (320)	0.22	HOMO→L+2 (90%)	$\pi-\pi^*$/CT
	4	4.20 (295)	0.17	HOMO→L+3 (89%)	CT
	5	4.29 (289)	0.01	HOMO→L+4 (94%)	CT
	6	4.66 (266)	0	HOMO–3→LUMO (85%)	$\pi-\pi^*$/n$-\pi^*$
	7	4.85 (256)	0.12	HOMO–1→LUMO (91%)	CT
	8	5.10 (243)	0	HOMO–2→LUMO (94%)	CT
L3	1	3.10 (400)	0.22	HOMO→LUMO (85%)	$\pi-\pi^*$/CT
	2	3.67 (338)	0.07	HOMO→L+1 (78%)	$\pi-\pi^*$/CT
	3	3.81 (325)	0.73	HOMO→L+2 (78%)	π-π^*/CT
	4	3.94 (314)	0.16	HOMO–1→LUMO (75%)	CT
	5	4.04 (307)	0.19	HOMO→L+3 (68%)	CT
	6	4.11 (302)	0.07	HOMO→L+4 (88%)	$\pi-\pi^*$/CT
	7	4.56 (272)	0.12	HOMO–1→L+1 (89%)	$\pi-\pi^*$/CT
	8	4.66 (266)	0	HOMO–3→LUMO (85%)	$\pi-\pi^*$/n-π^*
ReL1	1	3.24 (382)	0.28	HOMO→LUMO (77%)	$\pi-\pi^*$
	2	3.45 (359)	0.12	HOMO–1→LUMO (81%)	MLCT
	3	3.58 (347)	0.06	HOMO–2→LUMO (90%)	MLCT
	6	4.12 (301)	0.12	HOMO→L+2 (65%)	MLCT
	7	4.18 (296)	0.11	HOMO–1→L+1 (57%)	MLCT
	8	4.20 (295)	0.08	HOMO→L+3 (60%)	mixed
	16	4.55 (272)	0.05	HOMO–2→L+2 (58%)	MLCT
	26	4.91 (253)	0.12	HOMO–6→LUMO (62%)	mixed
	27	4.93 (251)	0.11	HOMO–3→L+4 (24%) HOMO–7→LUMO (35%)	MLLCT
ReL2	1	3.23 (384)	0.3	HOMO→LUMO (78%)	$\pi-\pi^*$
	2	3.44 (360)	0.11	HOMO–1→LUMO (83%)	MLCT
	3	3.57 (347)	0.06	HOMO–2→LUMO (90%)	MLCT
	6	4.12 (301)	0.12	HOMO→L+2 (63%)	MLCT/$\pi-\pi^*$
	7	4.18 (296)	0.05	HOMO–1→L+1 (40%)	MLCT/$\pi-\pi^*$
	8	4.19 (295)	0.15	HOMO→L+3 (47%)	MLCT/$\pi-\pi^*$
	18	4.56 (272)	0.05	HOMO–2→L+2 (44%)	MLCT
	25	4.85 (256)	0.05	HOMO–6→LUMO (56%)	MLCT
	26	4.88 (254)	0.1	HOMO–6→LUMO (24%) HOMO–7→LUMO (39%)	MLCT
	27	4.92 (252)	0.11	HOMO–3→L+4 (23%) HOMO–7→LUMO (45%)	MLCT
ReL3	1	2.89 (429)	0.18	HOMO→LUMO (94%)	CT
	2	3.35 (369)	0.06	HOMO–1→LUMO (61%) HOMO–2→LUMO (32%)	MLCT
	4	3.55 (349)	0.13	HOMO–2→LUMO (42%)	MLCT
	5	3.60 (344)	0.06	HOMO–3→LUMO (75%)	MLCT
	6	3.85 (322)	0.1	HOMO→L+2 (90%)	CT
	9	4.01 (309)	0.16	HOMO→L+4 (71%)	LMCT
	11	4.16 (298)	0.37	HOMO→L+5 (81%)	LMCT
	17	4.41 (281)	0.08	HOMO–1→L+2 (54%)	MLCT
	29	4.85 (255)	0.05	HOMO–6→LUMO (24%)	MLCT
ReL1py	1	3.25 (381)	0.36	HOMO→LUMO (85%)	$\pi-\pi^*$
	7	4.17 (297)	0.12	HOMO→L+3 (47%), MO→L+4 (41%)	MLLCT
	8	4.17 (297)	0.12	HOMO→L+3 (37%), HOMO→L+4 (45%)	MLLCT
	10	4.26 (291)	0.12	HOMO→L+5 (85%)	LLCT

Singlet $^1\pi-\pi^*$ emission is not commonly observed in metal complexes; rare examples have been reported.[19,45–47] The high decay rates of the free ligands ($\sim 5 \times 10^7$ s^{-1}) allow fluorescence from singlet states to compete with other processes. The result is a low quantum yield fluorescence; the $Re(CO)_3Cl$ unit acts

(47) Ley, K. D.; Whittle, C. E.; Bartberger, M. D.; Schanze, K. S. *J. Am. Chem. Soc.* **1997**, *119*, 3423–3424.

(48) Lees, A. J. *Chem. Rev.* **1987**, 711–743.

as a quencher of the free ligand fluorescence. Additionally, phosphorescence from a $^3\pi-\pi^*$ is observed as confirmed by the very long lifetime (falling in the sub-millisecond range) and vibronic coupling of the low-intensity bands.[48,49] The presence of a heavy atom, such as Re, increases spin–orbit coupling and thus intersystem crossing. For this reason, when the ligand is coordinated to the metal center, population of a $^3\pi-\pi^*$ state from the emissive $^1\pi-\pi^*$ state is favored. Singlet emissions of **ReL1** and **ReL2** are slightly blue-shifted with respect to the free ligand emissions; this is due to the forced *cis* conformation of the ligands. No low-energy bands are present in the **ReL3** spectrum, which has a broader ^{1}CT emission band red-shifted at 18.9×10^3 cm^{-1} (530 nm). The bigger Stokes shift of **ReL3** (6829 cm^{-1}) accounts for the higher CT character of the transition responsible for the emission, as observed in the case of **L3**.

HOMO → LUMO transition is responsible for the low-energy transition of the Re complexes. The HOMO shape of the three complexes can help to elicit the different photophysical behavior among them. As described previously, **ReL1** and **ReL2** have a small, but important, metal character in this orbital, which is responsible for causing intersystem crossing. Moreover, this aspect can also be described as a partial mixing of the $^1\pi-\pi^*$ state with MLCT states at higher energy.

Comparing the singlet geometries with the lowest-lying triplet state, which in all cases corresponds to the transition between the two frontier orbitals, gives interesting insights. Specifically, the torsional angle φ between the phenyl and the 1-pyridylimidazo[1,5-*a*]pyridine moieties (Scheme 1) decreases upon electron transfer from the HOMO to the LUMO. In particular, **ReL1** decreases by 7.74°, **ReL2** by 10.03°, and **ReL3** by 15.66°. The smaller distortion angle indicates that the triplet excited state relaxes toward a more planar geometry than in the ground state. Intersystem crossing should occur faster in the more twisted geometries of **ReL1** and **ReL2**.[10]

Photophysical Properties of ReL1py. To evaluate the effect of an ancillary ligand with donor properties on the dual fluorescence of **ReL1**, we substituted Cl with pyridine in **ReL1**. The choice was directed by the presence of a set of three Re(CO)$_3$Cl-based orbitals in proximity of the HOMO. **ReL3** has occupied frontier orbitals with ligand-based character, which make the complex less suitable for our purpose. Photophysical data and computed singlet excited states for **ReL1py** are summarized in Tables 2 and 3; Figure 5 reports the absorption and emission spectra of the complex. Two main bands are present in the absorption spectrum. The first band is at 297 nm and has a dominant MLLCT nature (Re(CO)$_3$py → **L1**). The lowest-energy band is due to a HOMO → LUMO transition. Orbitals are ligand-centered and have nearly the same character as the **ReL1**'s ones. Nevertheless, the HOMO has a reduced metal character with respect to the chloride derivative. Spin–orbit coupling is reduced as a result of this smaller contribution. In fact in the emission spectrum of **ReL1py**, the dual fluorescence has almost disappeared despite the similar quantum yield with respect to its Cl analogues. A singlet $^1\pi-\pi^*$ band (τ = 5.8 ns) centered at 22.9×10^3 cm^{-1} (437 nm) is dominating the spectrum, while only a small band, presumably a $^3\pi-\pi^*$ phosphorescence, remains at 17.9×10^3 cm^{-1} (559 nm). The energy difference between the emitting state and the closest MLCT (or better MLLCT) states is now bigger, causing less mixing than in the case of **ReL1**. The antiphase nature of the HOMO explains also the shortening of the Re−N bonds relative to the chelating ligand.

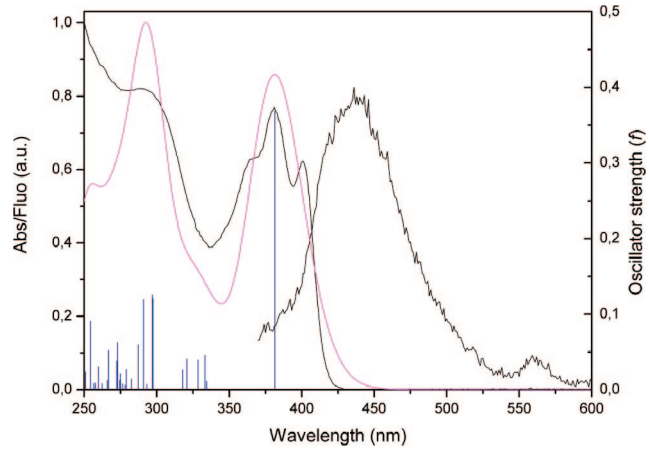

Figure 5. Experimental absorption and emission spectra of **ReL1py** (black line) in acetonitrile at room temperature. Calculated absorption spectrum for **ReL1py** in acetonitrile (magenta line). The excited states are shown as vertical bars with height equal to the extinction coefficient.

Electrochemistry. Cyclic voltammetry experiments on the free ligands and their rhenium complexes were performed in acetonitrile. The shape and energy of the HOMO (oxidation) and LUMO (reduction) orbitals determine the redox properties and potentials. On the oxidation side, **L1** and **L2** have a single reversible 1*e* oxidation at 0.42 and 0.40 V, respectively, while **L3** has two reversible oxidations at 0.18 and 0.35 V. As described previously, HOMOs for **L1** and **L2** are delocalized on the whole molecule. In the case of **L2**, there is no contribution from the *tert*-butyl group, thus explaining the very similar electrochemical behavior with respect to **L1** in oxidation. **L3** has a HOMO with a significant contribution from the dma group. The first oxidation peak can thus be centered on the dma group; the second peak may correspond to an oxidation process similar to the one of the other two ligands. All ligands have chemical irreversible multielectron reductions at very negative potentials. The peak potentials E_p (vs ferrocene) measured at a scan rate of 0.2 V/s are –2.81 V for **L1**, −2.79 V for **L2**, and −2.87 V for **L3**. All LUMOs are 1-pyridylimidazo[1,5-*a*]pyridine-based, without any contribution from the phenyl moieties.

Rhenium complexes display very similar redox properties. Reductions remain irreversible, since the LUMOs are practically unaltered by the coordination. However, the reduction processes become monoelectronic, pointing out that the electron-withdrawing properties of the Re moiety avoid the complete decomposition of the ligands after the reduction processes. In fact, they occur at less negative potentials (E_p at 0.2 V/s equal to −2.18, –2.18, and −2.19 V for **ReL1**, **ReL2**, and **ReL3**, respectively). Oxidations remain reversible and monoelectronic, but they fall, as expected by metal coordination, at higher potentials. **ReL1** and **ReL2** have a single oxidation process centered at $E_{1/2}(0/+1) = 0.89$ and 0.88 V, respectively, whereas **ReL3** shows two 1*e* reversible oxidation processes centered at $E_{1/2}(0/+1) = 0.55$ V and $E_{1/2}(+1/+2) = 0.81$ V. These features are consistent with HOMO orbitals of the same kind described for the ligands.

The redox properties of **ReL1py** are similar to those of **ReL1**, taking in account that the replacement of Cl by py makes **ReL1py** cationic. As a matter of fact, the positive charge shifts the reduction toward less negative potentials (E_p = –1.97 V at

(49) De Angelis, F.; Fantacci, S.; Sgamellotti, A.; Cariati, E.; Ugo, R.; Ford, P. C. *Inorg. Chem.* **2006**, *45*, 10576–10584.

0.2 V/s), but the process remains chemically irreversible up to a scan rate of 40 V/s. There are two subsequent oxidation processes, the first reversible occurring at $E_{1/2}(+1/+2) = 1.09$ V and the second chemically irreversible up to a scan rate of 40 V/s, located at $E_p = 1.56$ V (measured at a scan rate of 0.2 V/s). Both oxidations potential values of **ReL1py** are positively shifted in comparison with the corresponding values of **ReL1**. This is expected, because even though py has a better electron-donor properties than Cl, we add a positive charge on the metal complex.[50] However, in the case of **ReL1py**, the ligand-centered oxidation at $E_{1/2}(+1/+2) = 1.09$ V makes the metal-centered oxidation process (+2/+3) completely chemically irreversible due to the reduced electron density. These features are consistent with the computational results on **ReL1py**: the LUMO (+1/0 reduction) and the HOMO (+1/+2 oxidation) are both a π^* orbitals centered on the chelating part of the ligand, whereas the HOMO–1 (+2/+3 oxidation) is mainly centered on the $Re(CO)_3$ part of **ReL1py**.

Conclusions

In this paper, we reported the synthesis of new rhenium complexes and of a new 1-pyridylimidazo[1,5-*a*]pyridine ligand and the study of their photophysical properties. The use of DFT and TDDFT calculations was fundamental in elucidating differences among the investigated species in their electronic structures and their excited states. Ligands **L1** and **L2** show $^1\pi-\pi^*$ emission with limited charge-transfer character (CT), while **L3** emits from an excited state with higher CT character due to the presence of a dimethylamino group. **ReL1** and **ReL2**, although similar to their ligands, display a ligand-centered $^1\pi-\pi^*/^3\pi-\pi^*$dual emission. In the case of **ReL1py**, the dual fluorescence is almost gone as a result of reduced mixing between metal and ligand orbitals in the HOMO. Dual fluorescence at room temperature for **ReL1** and **ReL2** and **ReL1py** was explained by means of different metal contributions in the ligand-centered HOMOs. Finally, **ReL3** emits from a ligand-centered CT state. The X-ray structure of complex **ReL3** was solved and the electrochemical behavior of all ligands and complexes was explored. The 1-pyridylimidazo[1,5-*a*]pyridine ligands demonstrated to have good potential for optical application, since excited states of their metal complexes can be easily tuned by varying the substituents in position 3. For these reasons we are currently exploring the possibility of synthesizing new ligands with better donor–acceptor properties and of using other metal ions (such as osmium and iridium), more promising for optical applications, particularly as emitters in the blue region of the spectrum.

Acknowledgment. The authors acknowledge financial support of this work by Regione Piemonte and thank Tiziana Ruiu for helping in the preparation of Figure 4.

Supporting Information Available: Crystallographic data and CIF file for **ReL3**. This material is available free of charge via the Internet at http://pubs.acs.org.

OM701175Z

(50) Albertino, A.; Garino, C.; Ghiani, S.; Gobetto, R.; Nervi, C.; Salassa, L.; Rosenberg, E.; Sharmin, A.; Viscardi, G.; Buscaino, R.; Milanesio, M.; Croce, G. *J. Organomet. Chem.* **2006**, *692*, 1377–1391.